Geotech Geol Eng
https://doi.org/10.1007/s10706-020-01509-w

ORIGINAL PAPER

Pullout Behavior of Sensor-Enabled Geobelts in Weathered Rock Material–Granulated Rubber Mixtures

Yi-lin Wang · Xin-zhuang Cui · Jin Li · Lei Wang · Jun Li · Jun-wei Su

Received: 30 October 2019 / Accepted: 4 August 2020

Abstract As lightweight materials, granulated rubber–weathered rock material (WRM) mixtures could be utilized as backfills in geosynthetics reinforcement structures to reduce deformations. However, the deformation behaviour of geosynthetics in granulated rubber–WRM mixtures is not clear. In this paper, pullout tests considering different normal pressures (30 kPa, 50 kPa and 100 kPa) and different granulated rubber contents (10%, 15% and 30%) are performed. Sensor-enable geobelts (SEGB) are employed, which can realize distributed measurements on the strains of SEGB inside soil. Two constitutive models—bilinear model and hyperbolic model are established based on tensile tests and direct shear tests to capture the full stress–strain curves and the interfacial shear responses, respectively, and are employed in the derivation of load transfer equation for pullout process. Numerical results of load transfer equation give distributions of tensile forces, strains, displacements and shear stresses. Test results validate the established constitutive models. Rubber content has an optimal value for the best geobelt–soil interaction. The deformations of geobelts in pullout process start from the front end, but decrease rapidly in soil. Under high normal pressures, the front part of geobelts exhibit quasi-plasticity. The shear stress distributes more uniformly under low normal pressure.

Keywords Geosynthetics · Granulated rubber · Weathered rock material · Pullout test · Hyperbolic model

Y. Wang · X. Cui (✉) · L. Wang · J. Li · J. Su
School of Civil Engineering, Shandong University, Jinan 250061, People's Republic of China
e-mail: cuixz@sdu.edu.cn

Y. Wang
e-mail: eason_wyl@163.com

L. Wang
e-mail: wanglei@sdu.edu.cn

J. Li
e-mail: forzaapis@126.com

J. Su
e-mail: 1571201036@qq.com

J. Li
Shandong Jiaotong Univiersity, Jinan 250357, People's Republic of China
e-mail: sdzblijin@163.com

List of symbols

α	Coefficient of tensoresistivity (−)
β	Coefficient of tensoresistivity (−)
ε	Strain of geobelt (%)
ε_u	Strain level of inflection point in bilinear model (%)
φ_w	Internal friction angle of weathered rock material (°)
φ_{sg}	Angle of interfacial friction (°)
σ	Stress of geobelt (Pa)
σ_u	Stress level of inflection point in bilinear model (Pa)

Published online: 18 August 2020

σ_v Normal pressure (Pa)
τ Shear stress of geobelt (Pa)
τ_f Shear failure strength of geobelt (Pa)
τ_{ul} Ultimate value of shear stress of geobelt (Pa)
a Parameter in hyperbolic model (m/Pa)
A Area of cross section of geobelt (m^2)
b Parameter in hyperbolic model (Pa^{-1})
B Intercept of second line in bilinear model (Pa)
C_c Coefficient of curvature (−)
c_{sg} Apparent cohesion (Pa)
C_u Uniformity coefficient (−)
c_w Cohesion of weathered rock material (kPa)
E_1 Slope of first line in bilinear model, i.e. elastic modulus (Pa)
E_2 Slope of second line in bilinear model (Pa)
E_i Initial modulus of interfaces (Pa/m)
F Tensile force of geobelt (N)
F_0 Front pullout force of geobelt (N)
F_{0m} The maximum value of front pullout force (N)
h Non-dimensionalized discretized element length (−)
k Intercept of normalized initial modulus-normal pressure curve (m^{-1})
l Length of geobelt (m)
n Number of discretized elements (−)
p Slope of normalized initial modulus-normal pressure curve (−)
p_a Atmospheric pressure (Pa)
R_s Measured value of electrical resistance (Ω)
R_0 Initial value of electrical resistance (Ω)
R_{uf} Shear failure ratio of shear stress (−)
t Thickness of geobelt (m)
U Normalized displacement (−)
u Displacement of geobelt (m)
u_m Maximum value of pullout displacement (m)
w Width of geobelt (m)
X Normalized length of geobelt (−)
x_u Coordinate of inflection point (m)

1 Introduction

Benefitting from the competent interaction between geosynthetics and surrounding soils, geosynthetics reinforced structures (GRS) have excellent performances in terms of increasing the stability and stabilizing the earth structures as well as improving serviceability by reducing the settlement and lateral displacements, and have been extensively employed in geotechnical engineering practice to reinforce soils and improve the overall performance of foundation (Chen and Abu-Farsakh 2016; Shahin et al. 2017; Yu and Bathurst 2017), embankments (Chawla and Shahu 2016; Liu et al. 2017; Shen et al. 2018), and walls (Liu 2016; Yu et al. 2016; Zhang et al. 2018). The deformation of geosynthetics is one of the important indexes to evaluate the overall performances of GRS, which, however, is generally difficult to analyze both in theoretically and practically.

Theoretically, the deformation of geosynthetics is highly involved in the constitutive models of geosynthetic-soil interfacial behaviors. Extensive research has demonstrated that interfacial behaviors vary with the types of both geosynthetics and soils (Infante et al. 2016). Rousé et al. (2014) reported that two different interfacial responses (hardening and softening) were observed in the interaction of two different textured planar inclusions embedded in sand. Wang et al. (2016) found that soils at interfaces all showed hardening responses for geobelts (geogrids without transvers ribs) although softening was also observed for other geogrids under the same stress condition. Many researchers have reported the interfacial shear stresses showing hardening response with shear displacements (e.g., Gurung and Iwao 1999; Punetha et al. 2017; Sadat Taghavi and Mosallanezhad 2017), while the softening responses were mostly observed in the interaction between geosynthetics and clayey soils (e.g. Chai and Saito 2016).

In practice, however, the soil used in some GRS engineering is much more complicated. The highway construction in China has extended from plain area to hilly area, where high-quality backfilling material for the highway embankments is not always available on site but the use of weathered rock materials (WRM) on site can give significant savings. Although WRM has advantages such as high compression strength and good impermeability, the compactibility and durability of WRM are unsatisfied to the needs of practical engineering (Huang 2017). If WRM could participate in the embankment construction as backfilling materials, massive land resources could be conserved. Recent research has shown that the compactibility, durability and shear strength of the soil could be improved by mixing with shredded, granulated or powdered rubbers mechanically reduced from scrap

tires (Ghazavi 2004; Attom 2006; Anastasiadis et al. 2012; Argyroudis et al. 2016; Shrestha et al. 2016; Cui et al. 2017). As one of the massive wastes from automotive industry, scrap tires would be hazardous to the ecological environment if disposed with traditional methods such as stacking in landfills and burning in power plants. It has been considered to be one of the environment-friendly disposal methods for shredded rubber to be mixed with soil and utilized as engineering backfilling materials. Being lightweight and easy to be compacted, the shredded rubber-soil mixtures have been widely accepted in many geosynthetics reinforcement structures such as reinforced embankments (Bosscher et al. 1997) and reinforced foundations (Tafreshi et al. 2014). Clearly, the geosynthetics-soil interfacial behaviour is highly related to the property of WRM-shredded rubber mixtures. It is necessary to investigate the interfacial behaviour between the geosynthetics and mixtures, especially the deformation of geosynthetics.

Pullout test is effective to analyze the geosynthetics–soil interaction. Some researchers have investigated the pullout behaviour of geosynthetics in shredded rubber-soil mixtures. Bernal et al. (1997) conducted pullout tests on three types of flexible geogrids to determine the interaction coefficients between geogrid reinforcement and fill material. Pure shredded tires and rubber–sand mixtures were used as fill materials. From the test results, it is obvious that the interaction coefficients between the shredded tire fill and the geogrid were lower than common interaction coefficients between soil and geogrid obtained from the previous researchers. Tanchaisawat et al. (2010) investigated the interaction between geogrid and tire chip-sand backfill with different mixing ratios by numerous tests, including index tests, compaction tests, pullout tests, and large-scale direct shear tests, to evaluate the effect of the tire chip ratio on the interaction characteristics Balunaini et al. (2014). performed pullout tests of uniaxial geogrids in shredded tire-sand mixtures and investigated the effects of shredded tire diameter, mixing ratio, and normal pressure on the geogrid-mixture interaction. However, many researchers focused on external indices of pullout tests such as pullout forces, front displacements and shear strength. The internal indices of pullout tests such as the deformations and stresses of geosynthetics inside soil were lack in pullout test analysis.

Practically, the deformation of geosynthetics in GRS is difficult to acquire precisely due to the limitations of current measurement methods. Efforts have been made to measure the deformations of the geosynthetics inside the soil. Fiber Bragg grating (FBG) sensors (Chen et al. 2016), strain gauges (Wang et al. 2015), LVDTs (Wang et al. 2016) and dial gauges (Tavakoli et al. 2016) are common methods in many tests to measure the deformations of the geosynthetics inside the soil, but these measurements have defects to some degree such as the effect of the installation on the geosynthetics–soil interfaces and the inconvenience of the measurements for in situ tests. Recently, a novel concept of sensor-enabled geobelts (SEGB) based on the tensoresistivity of conductive polymers has been successfully manufactured by Cui et al. (2018a, b). The tensoresistivity of SEGB makes it easy to analyze the deformations of geobelts in soil. Taking advantage of the tensoresistivity, the self-measurement of SEGB could obtain the deformation distribution inside the soil.

This paper presents analysis on SEGB interacted with the WRM-granulated rubber mixture. Granulated rubber are added into WRM with mass ratios of 10%, 15% and 30%, respectively. Sensor-enable geobelts (SEGB) are tested with mixtures in direct shear tests and pullout tests. Load transfer equation for pullout process is established based on two constitutive models—the bilinear model capturing the full stress–strain response of geobelt and the hyperbolic model simulating the geobelt–soil interaction. The pullout tests are carried out with granulated rubber-WRM mixtures via a self-developed testing apparatus with the normal pressures of 30 kPa, 50 kPa and 100 kPa, respectively. The proposed models are validated by comparing the numerical results and measured results from tests, including the self-measurement of SEGB. The effect of granulated rubber content on the pullout behavior of SEGB is discussed, and the deformation behaviors of geobelts in pullout process are analyzed.

2 Testing materials

2.1 Sensor-enabled Geobelts (SEGB)

A novel concept of sensor-enabled geobelt (SEGB) was employed in this paper. Initially developed by Hatami et al(2009) and successfully manufactured by

the authors (Cui et al.2018a,b; Li et al. 2018), SEGB is a composite made from polymeric material—conductive carbon black dispersed in high-density polyethylene (HDPE). The geometrical and strength properties of SEGB are presented in Table 1.

It is noted that the products of SEGB manufactured from factory are in thin plate shape with 0.5 m wide, which could be easily cut to be geobelts or geogrids as required. To enhance the frictions between SEGB and soil, the texture of SEGB was designed as rhombuses with long and short diagonals of 4.0 mm and 1.5 mm, respectively, as shown in Fig. 1.

The conductive carbon black dispersed in HDPE allows the SEGB to exhibit tensoresistivity, which enables the strains of SEGB to be acquired through measuring the changes of electrical resistance. Provided as a new method to determine the strain of geobelts, the tensoresistivity was the most remarkable advantages of SEGB Cui et al. (2018a,b) conducted tests on tensoresistivity performance and suggested the strain determination method as follows:

$$\frac{R_s}{R_0} = \alpha\varepsilon^2 + \beta\varepsilon + 1 \quad (1)$$

where ε is the strain of SEGB; R_0 is initial value of electrical resistance; R_s is measured value of electrical resistance after deformation; and the coefficients α and β are constants, which are only related to the materials. In this case, $\alpha = 0.016$ and $\beta = 0.185$.

The SEGB specimens used in uniaxial tensile tests were 100 mm long and 25 mm wide. The effective length and width of specimens employed in pullout tests were 600 mm and 40 mm, respectively. By attaching wires, it is available to measure the electrical resistance between two adjacent attached nodes, as shown in Fig. 2. The attached nodes were encircled with conductive adhesive tapes. The wires that attached to specimens were connected to ohmmeters

Table 1 Geometrical and strength properties of SEGB

Properties	Unit	Value
Mass/unit area	kg/m^2	1.48
Thickness	mm	1.80
Tensile strength	kN/m	21.6
Loading at 2% strain	kN/m	10.3
Breaking elongation	%	17.0

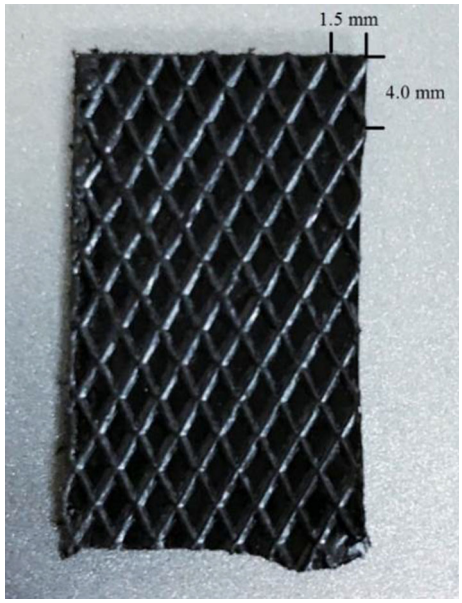

Fig. 1 Material of SEG: rhombuses texture of surface (Reproduced from Cui et al. 2018a)

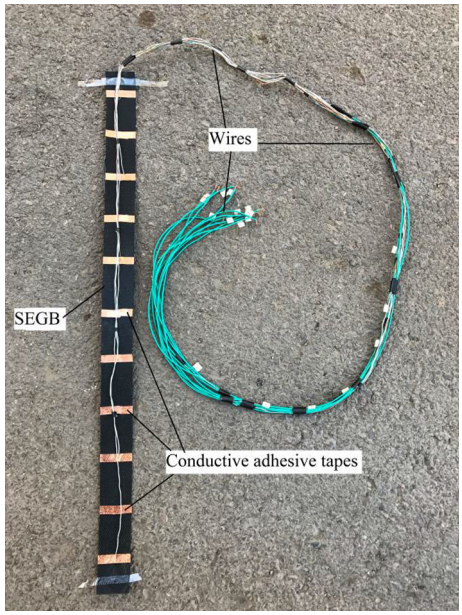

Fig. 2 SEGB specimen with wires and conductive adhesive tapes (Reproduced from Cui et al. 2018a)

to measure the electrical resistance values. There were 11 measuring points uniformly distributed along the specimen with the space of 60 mm. Note that the

electrical resistance values must be measured between adjacent measuring points.

2.2 Testing Soil

The testing soil employed in this paper is the mixture of weathered rock materials and shredded rubbers.

The weathered rock material (WRM) is from Xintai Area in Shandong Province, China. The main mineral composition is mica, hornblende, quartz, plagioclase, etc. The WRM is SP (as per Unified Soil Classification System ASTM D422-63) with d_{10} = 0.13 mm, d_{30} = 0.45 mm, d_{50} = 1.01 mm, d_{60} = 1.76 mm, uniformity coefficient C_u = 13.5 and coefficient of curvature C_c = 0.89. The particle size distribution is shown in Fig. 3. The maximum dry density and the optimal moisture content are 2.10 g/cm^3 and 9.3%, respectively. The cohesion c_w and the internal friction angle φ_w of WRM are 14.43 kPa and 25.99°, respectively, under the relative density of 95%. Although WRM is classified as SP, the cohesion c exists but small.

According to *ASTM D6270-17*, shredded rubber refers to pieces of scrap tires resulting from mechanical processing. The shredded rubbers used in tests are non-spherical particles with average diameter of 2 mm, classified as granulated rubbers. The particle size distribution is illustrated in Fig. 3.

The WRM in the mixture was dry and compacted with a relative density of 95%. According to ASTM D6270, the shear strength of mixtures would be reduced once the mass ratio of granulated rubber exceeded 30%. Therefore, the mass ratios of granulated rubbers in the mixtures were 10%, 15% and 30%, respectively.

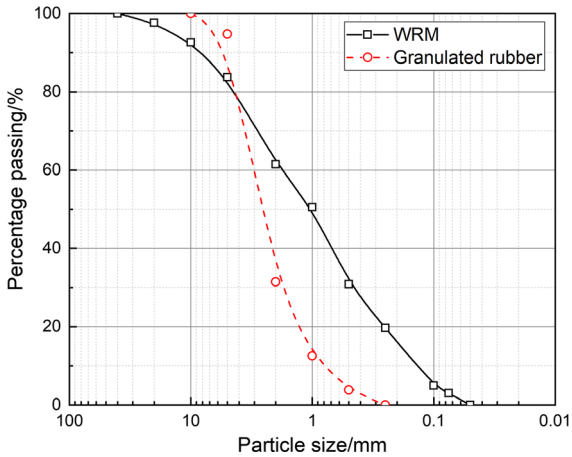

Fig. 3 Particle size distribution of the weathered rock materials and granulated rubbers

3 Tensile property of geobelts and bilinear model

Traditionally, the geosynthetics in pullout tests were usually analyzed as elastic materials. Madhav et al. (1998) proposed a theoretical model with the Gauss-Siedel iteration numerical method used for pullout tests. Gurung (2001) derived a 1-D nonlinear equation in pullout tests and conducted parametric numerical analysis in non-dimensional terms. Racana et al. (2003) conducted numerical analysis in pullout tests on corrugated geotextile strips. Abdelouhab et al. (2010) studied the behaviors of metallic and synthetic strips in pullout tests. The geosynthetics in these studies were analyzed under the assumption that geosynthetic material is purely elastic. Such assumption could only be accepted for initial pullout process, in which the geosynthetics showed limited deformations. As kind of polymeric material, geosynthetics must be considered in quasi-plastic model with large deformation.

To obtain stress–strain curves of SEGB, uniaxial tensile tests were conducted on universal testing machine. The tensile loading speed was 1.0 mm/min as per *ASTM D6637-01*. Figure 4 shows the full stress–strain curve of SEGB.

The full stress–strain curve could be divided into two stages. In stage 1, the stress of SEGB increased

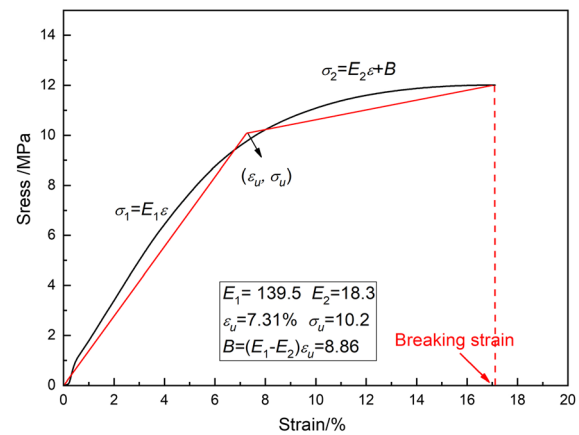

Fig. 4 Full stress–strain curve of SEGB in a uniaxial tensile test

rapidly with strain increasing due to high stiffness. In stage 2, the stress increased slowly with strain developing due to smaller stiffness than that in stage 1. In pullout tests with high normal pressures, SEGB can very likely develop into stage 2. In this study, the stress–strain curve of SEGB could be approximately described with the following bilinear relation:

$$\sigma = \frac{F}{A} = \begin{cases} E_1\varepsilon, & \varepsilon < \varepsilon_u \\ E_2\varepsilon + B = E_2\varepsilon + (E_1 - E_2)\varepsilon_u, & \varepsilon \geq \varepsilon_u \end{cases} \quad (2)$$

where σ is axial stress of geobelt; E_1 is the slope of first line, i.e. elastic modulus; E_2 is the slope of second line; A is the cross section area of geobelt; B is the intercept of second line; F is the tensile force;$\sigma_u = E_1 \cdot \varepsilon_u$, and point ($\varepsilon_u$, σ_u) is the intersection point for two lines.

Based on results of uniaxial tensile tests, the parameters in Eq. (2) can be obtained: E_1 = 139.5 MPa, E_2 = 18.3 MPa, ε_u = 7.31%, σ_u = 10.2 MPa. It is difficult to directly acquire the coordinates of the intersection point (ε_u, σ_u) from Fig. 4. Chari and Meyerhof (1983) provided an alternative method to find the intersection point. By converting the strain axle in Fig. 4 into logarithm type, the shape of full stress–strain curve changes and there might be a turning point as Fig. 5. shows. The turning point could be adopted as the intersection point.

4 Geobelt–soil interaction and hyperbolic model

Pullout tests could be considered as a combination of the uniaxial tensile test and direct shear test. When a geobelt is pulled out from confining soil, the geobelt–soil interfacial shear stress acting along the geobelt length is mobilized once the pullout force is applied on geobelt. It is necessary to investigate the geobelt–soil interfacial response.

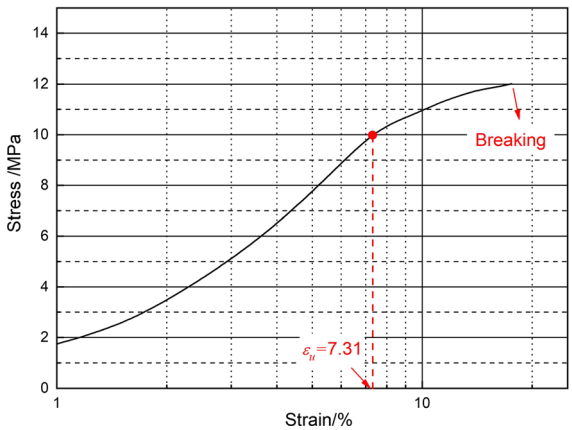

Fig. 5 Full stress–strain curve of SEGB in logarithm coordinate

4.1 Testing apparatus

Direct shear tests were carried out to investigate the interfacial response between SEGB and the mixtures. The normal pressure was applied from a leverage system on the fixed upper shear box, while the lower shear box could horizontally move with low-friction stainless steel balls on two tracks. The maximum displacement of the lower shear box was 20 mm, and measured by dial gauges. The SEGB specimens were cut into disks with diameter of 61.8 mm, which could cover the direct shear area between the upper and lower shear boxes. The testing specimens were laid on the compacted mixtures in the lower shear box to guarantee that the specimens did not slide during the tests and the surface of specimen was consistent with shearing area. As per *ASTM D5321/D5321M-19*, direct shear tests were conducted with a constant displacement rate of 1.0 mm/min under the normal pressures of 30 kPa, 50 kPa and 100 kPa.

4.2 Direct shear test results and hyperbolic model for geobelt–soil interaction

Figure 6 shows the results of direct shear tests: (a) Shear stress–shear displacement curve, and (b) Shear strength-normal pressure curve. It is observed that the interfacial shear stresses increased with the increasing displacements. The shear stresses increased rapidly at early stage, but slowly afterwards. In this study, the shear stress-displacement curves in Fig. 6a can be described as the following hyperbolic relation:

$$\tau = \frac{u}{a + bu} \quad (3)$$

where a and b are the parameters, which was only related to the shear interfaces.

Considering that the Duncan-Chang model (1970) of soil is also a hyperbolic model, the similar methods could be used to determine parameters a and b.

In Fig. 6a, the slope of tangent line at the original point is called initial modulus of interfaces, E_i. Taking the derivative of Eq. (3):

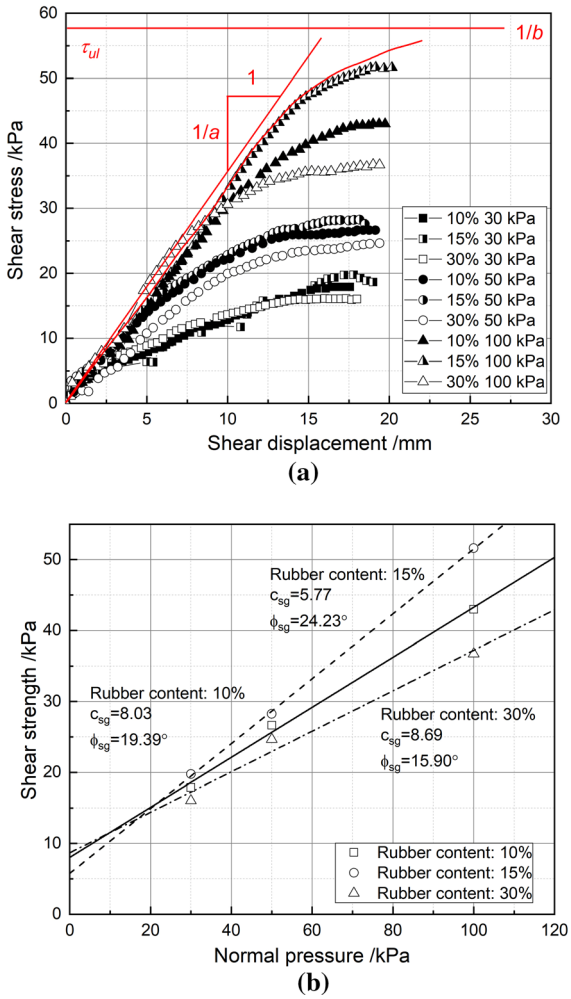

Fig. 6 Results of direct shear tests: **a** Shear stress–shear displacement curve; **b** Shear strength-normal pressure curve

$$E_{\mathrm{i}}=\left.\frac{\mathrm{d}\tau}{\mathrm{d}u}\right|_{u=0}=\frac{1}{a} \tag{4}$$

E_{i} is not a constant, which varies with normal pressure σ_v. If normalized with atmospheric pressure p_{a} as $\frac{E_{\mathrm{i}}}{p_{\mathrm{a}}}$ and $\frac{\sigma_{\mathrm{v}}}{p_{\mathrm{a}}}$, there exists linear relationship between the normalized E_{i} and σ_{v} expressed as:

$$\frac{E_i}{p_{\mathrm{a}}}=k\left(\frac{\sigma_{\mathrm{v}}}{p_{\mathrm{a}}}\right)^{p} \tag{5}$$

where k and p are constants decided by tests that can be determined by the intercept at $\sigma_{\mathrm{v}}/p_{\mathrm{a}} = 1.0$ and the tangent values of $E_{\mathrm{i}}/p_{\mathrm{a}}$, respectively.

When displacement u approaches to the Infinity, Eq. (3) is expressed as follows:

$$\tau_{\mathrm{ul}}=\lim_{u\to\infty}\tau=\lim_{u\to\infty}\frac{u}{a+bu}=\frac{1}{b} \tag{6}$$

where τ_{ul} is the limit value of τ, which refers to the hyperbolic asymptote value.

The real maximum value of interfacial shear stress is usually less than the hyperbolic asymptote value. Therefore, Eq. (6) can also be expressed as:

$$b=\frac{1}{\tau_{\mathrm{ul}}}=\frac{R_{\mathrm{uf}}}{\tau_{\mathrm{f}}} \tag{7}$$

where R_{uf} is the shear failure ratio of shear stress; and τ_{f} is the shear failure strength.

R_{uf} can be determined by back-calculation of direct shear test results. τ_{f} could be determined by τ_{f} -σ_{v} curve shown in Fig. 6b. τ_{f} -σ_{v} curve can be linearly fitted as follows:

$$\tau_f=c_{sg}+\sigma_v\cdot\tan\varphi_{sg} \tag{8}$$

where c_{sg} is the apparent cohesion and is equal to the intercept of the line; and φ_{sg} is the angle of interfacial friction, whose tangent value is equal to the slope of the line.

Based on the results of direct shear tests, the parameters in the hyperbolic model are tabulated in Table 2. It could be seen from Table 2 that the mass ratio of granulated rubbers in the mixtures had limited influences on the apparent cohesion c_{sg}. However, when the mixture contained 15% granulated rubbers, the angle of interfacial friction φ_{sg} was significantly higher than the other two mixtures. The value of E_i in the mixture of 15% mass ratio was also higher than the other two mixtures under the same normal pressure.

5 The load transfer equation in pullout tests

Pullout behaviour of geobelts is closely related to the tensile property of the geobelts and the geobelt–soil interaction. Obtained from uniaxial tensile tests, the stress–strain curves of geobelts and the derived bilinear model are related to the mechanical characteristics of the material rather than the testing surroundings. Although the geobelts are tested under different surroundings in uniaxial tensile tests and pullout tests, the established bilinear equation of stress–strain curves (Eq. 2) and the hyperbolic equation of geobelt–soil interaction (Eq. 3) could be

Table 2 The hyperbolic parameters determined from direct shear test results

Mass ratio of granulated rubber%	σ_v (kPa)	E_i (kPa/mm)	c_{sg} (kPa)	φ_{sg} (°)
10	30	2.08	8.03	19.39
	50	3.13		
	100	4.00		
15	30	2.50	5.77	24.23
	50	3.33		
	100	4.20		
30	30	2.32	8.69	15.90
	50	2.85		
	100	3.85		

directly employed in the deformation analysis of the SEGB element in pullout tests.

5.1 Load transfer equation in pullout tests

Figure 7 shows a small differential geobelt element of length dx. When a geobelt is pulled out from soil under normal pressure σ_v, the pullout force F_0 mobilizes the shear stresses τ acting along the geobelt–soil interfaces. The mechanical equilibrium of the geobelt element gives:

$$dF(x) = -2w\tau(x)[1 + \varepsilon(x)]dx \tag{9}$$

where $F(x)$ is the tensile force of the element; $\varepsilon(x)$ is the strain of the element; and w is the width of the geobelt.

The definition of strain gives:

$$\varepsilon(x) = -\frac{du(x)}{dx} \tag{10}$$

where $u(x)$ is the displacement of the element.

Combining the Eqs. (2), (3), (9) and (10), the load transfer equation of geobelt in pullout process could be acquired:

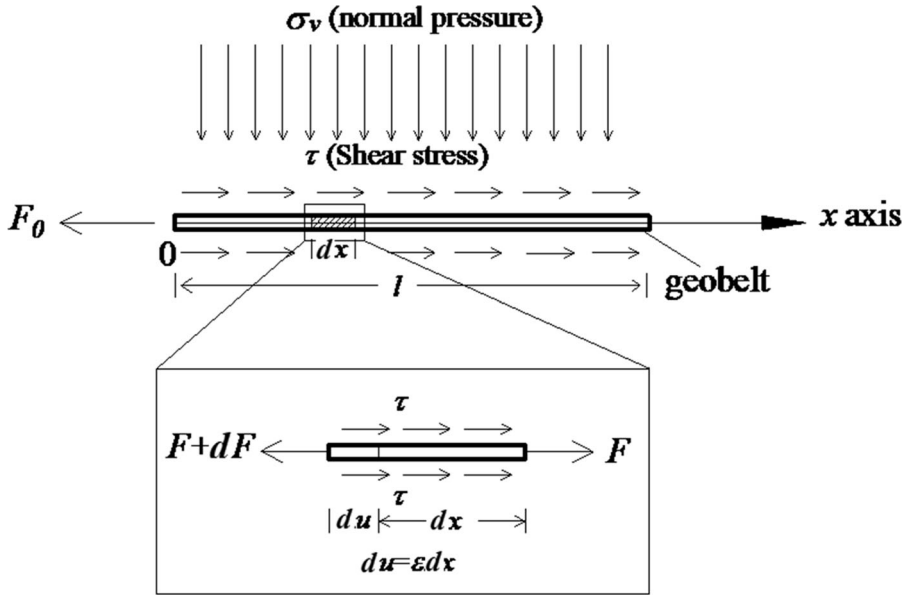

Fig. 7 Free-body diagram of geobelt element in pullout tests

$$\frac{\mathrm{d}^2u(x)}{\mathrm{d}x^2}+\frac{2w}{E_2t}\frac{u(x)}{a+bu(x)}\left[\frac{\mathrm{d}u(x)}{\mathrm{d}x}-1\right] = 0 \text{ for } x\le x_u \text{ or } \varepsilon\ge\varepsilon_u \tag{11}$$

where $t = A/w$, the thickness of geobelt; $\frac{\mathrm{d}u(x)}{\mathrm{d}x} = -\frac{1}{E_2}\left[\frac{F(x)}{A}-B\right]$, and $B = \left(1-\frac{E_2}{E_1}\right)\sigma_u$

$$\frac{\mathrm{d}^2u(x)}{\mathrm{d}x^2}+\frac{2w}{E_1t}\frac{u(x)}{a+bu(x)}\left[\frac{\mathrm{d}u(x)}{\mathrm{d}x}-1\right] = 0 \text{ for } x>x_\mathrm{u} \text{ or } \varepsilon<\varepsilon_\mathrm{u} \tag{12}$$

where $\frac{\mathrm{d}u(x)}{\mathrm{d}x} = -\frac{F(x)}{E_1A}$.

e boundary conditions of load transfer equation are:

$$\begin{aligned} &F(x) = \mathrm{F}_0 \text{ or } \frac{\mathrm{d}u(x)}{\mathrm{d}x} = -\frac{1}{E_2}\left(\frac{F_0}{A}-B\right), && \text{at } x=0\\ &F(x) = 0 \text{ or } \frac{\mathrm{d}u(x)}{\mathrm{d}x} = 0, && \text{at } x=l \end{aligned} \tag{13}$$

where F_0 is the pullout force in pullout test results.

Equations (11) and (12) can be non-dimensionalized and simplified to:

$$\frac{\mathrm{d}^2U(X)}{\mathrm{d}X^2}+\frac{2l^2}{E_2t}\frac{U(X)}{a+bu_mU(X)}\left[\frac{u_m}{l}\frac{\mathrm{d}U(X)}{\mathrm{d}X}-1\right] = 0 \tag{14a}$$

and

$$\frac{\mathrm{d}^2U(X)}{\mathrm{d}X^2}+\frac{2l^2}{E_1t}\frac{U(X)}{a+bu_mU(X)}\left[\frac{u_m}{l}\frac{\mathrm{d}U(X)}{\mathrm{d}X}-1\right] = 0 \tag{14b}$$

where $U = \frac{u(x)}{u_m}$ and $X = \frac{x}{l}$; u_m is the maximum value of pullout displacement.

The boundary conditions in non-dimensionalized form become:

$$\begin{aligned} &F(X) = F_0 \quad \text{or} \quad \frac{\mathrm{d}U(X)}{\mathrm{d}X} = -\frac{1}{E_2u_m}\left(\frac{F_0}{A}-B\right), \quad at \quad X=0,\\ &F(X) = 0 \quad \text{or} \quad \frac{\mathrm{d}U(X)}{\mathrm{d}X} = 0 \qquad\qquad at \quad X=1 \end{aligned} \tag{15}$$

5.2 Numerical solutions by finite-differential method

Combined with the boundary conditions, Eqs. (14a) and (14b) are nonlinear differential equations of the Boundary Value Problem (BVP), which cannot be solved analytically. Finite-differential method could be used for numerical solutions through following steps:

Step 1 discretizing the geobelt into n elements with the proportion of each element, $h = 1/n$, and replacing the derivatives with backward differentials:

$$\begin{cases} \dfrac{\mathrm{d}U(X)}{\mathrm{d}X} &= \dfrac{U_{i+1}(X)-U_i(X)}{h}\\ \dfrac{\mathrm{d}^2U(X)}{\mathrm{d}X^2} &= \dfrac{U_{i-1}(X)-2U_i(X)+U_{i+1}(X)}{h^2}\\ i\in[0,\mathrm{n}] \end{cases} \tag{16}$$

Then the Eqs. (14a) and (14b) could be translated into difference form as follows:

$$U_{i-1}(X)-2U_i(X)+U_{i+1}(X) = -\frac{2h^2}{E_2t}\varphi\left[U_i(X),\frac{U_{i+1}(X)-U_i(X)}{h}\right] \tag{17a}$$

$$U_{i-1}(X)-2U_i(X)+U_{i+1}(X) = -\frac{2h^2}{E_1t}\varphi\left[U_i(X),\frac{U_{i+1}(X)-U_i(X)}{h}\right] \tag{17b}$$

where

$$\varphi\left[U_i(X),\frac{U_{i+1}(X)-U_i(X)}{h}\right] = \frac{U_i(X)}{a+bu_mU_i(X)}\left[\frac{u_m}{l}\frac{U_{i+1}(X)-U_i(X)}{h}-1\right] \tag{18}$$

Step 2 to solve the displacement at node $i = n$, a fictitious node $i = n + 1$ next to the end of geobelt (at the node $i = n$) was assumed. The displacements at these nodes can easily be derived with the boundary condition as follows:

$$\begin{cases} \dfrac{U_1(X)-U_0(X)}{h} &= -\dfrac{l}{u_mE_2}\left(\dfrac{F_0}{A}-B\right)\\ \dfrac{U_{n+1}(\mathrm{X})-U_n(\mathrm{X})}{h} &= 0 \end{cases} \tag{19}$$

Combined with Eqs. (17a), (17b), (18) and (19), normalized displacement distribution along the geobelt, U_i, could be obtained.

Step 3 from the known displacements along the geobelt length, the strain, ε_i, at node i, could be calculated as follows:

$$\varepsilon_i = \frac{u_m}{l}\frac{U_{i-1} - U_{i+1}}{2h} \tag{20}$$

Step 4 the tensile force, F_i, and the interfacial shear stress, τ_i, at node i, could be calculated by Eqs. (2) and (3), respectively.

6 Pullout tests on SEGB in WRM-granulated rubber mixtures

The pullout device (as shown in Fig. 8) had four components: test chamber, horizontal pulling system, vertical loading system, and force sensor system. The SEGB specimen was embedded in compacted sand in the 800 mm-long × 400 mm-wide × 550 mm-high test chamber. The front end of the SEGB specimen extended through a gap in the front wall of the test chamber and was fixed on a clamp. A 100 mm-wide sleeve was used at the gap to reduce the pressure on front wall. Sponges were adhered between the sleeve pieces to prevent the loss of soil particles. The inner sides of the sidewalls were greased and then covered with plastic film to reduce the friction due to the mixture particles.

The system for applying the pulling load to the SEGB involved a driving screw powered by an electric servomotor. The servomotor ensured that the clamp moved at a constant displacement rate set as 1.0 mm/min as per *ASTM D6706*. The SEGB was clamped between two rubber sheets which were held between two steel plates by five high-strength bolts. No SEGB broke at the plates suggesting that the connection system did not bias the results.

The vertical loading system comprised a hydraulic jack attached to a reaction frame on one end and two I-beams on the other end. The two I-beams with a length of 600 mm were deployed abreast on a bearing plate to apply a normal pressure as uniform as possible. The bearing plate is a 10 mm-thick steel plate to cover the test chamber.

The force sensor system comprised two force sensors. One of the sensors monitored the tension induced by the screw in the horizontal pulling system; the other sensor was attached to vertical loading system to monitor the pressure from hydraulic jacks.

The WRM-granulated rubber mixture was compacted to a relative density of 95% in 50-mm thick layers, until the soil surface was slightly higher than the lower edge of the gap on test chamber. The SEGB specimen was laid on the soil with its front end firmly connected to the clamp by bolts and the wires run out of the test chamber for monitoring. The rest soil were compacted to the same relative density. The normal

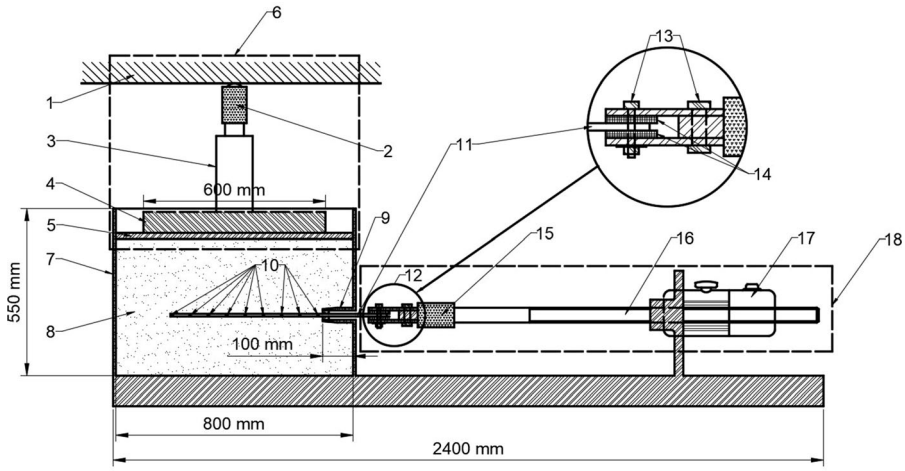

Fig. 8 Schematic of pullout test apparatus: 1-Reaction frame; 2-Pressure sensor; 3-Hydraulic jack; 4-I-beams; 5-Bearing plate; 6-Vertical loading system; 7-Test chamber; 8-Testing soil; 9-Sleeve (with sponges); 10-Conductive adhesive tapes; 11-Testing specimen; 12-Clamp; 13-High strength bolts; 14-Rubber sheet; 15-Tension sensor; 16-Driving screw; 17-Electric servomotor; 18-Horizontal pulling system

pressures in the pullout tests were 30 kPa, 50 kPa and 100 kPa. The test cases are summarized in Table 3.

7 Results and discussion

7.1 Front pullout force–displacement curves

The specimens were pulled out from mixtures under the normal pressure of 30 kPa, while broken under the normal pressures of 50 kPa and 100 kPa. Figure 9 illustrates the comparisons of numerical and tested pullout force–displacement curves with different rubber contents. Obviously, for the cases of normal pressures of 30 kPa and 50 kPa, the calculated front displacements were slightly larger than the tested results for the same level of front pullout force. However, for the cases of 100 kPa normal pressure, the calculated front displacements were slightly smaller than the tested results. These calculation errors might derive from the fitting errors in the bilinear model. Despite of this, the numerical calculations generally agreed well with the tested results, indicating that the bilinear model capturing the full stress–strain curves of SEGB and the hyperbolic model simulating the interfacial responses are effective.

Both of tested and numerical results have indicated that the increasing normal pressure would result in faster increment of front pullout force, or smaller front displacement to reach the maximum value of front pullout force. For all the pullout cases of breaking, the SEGB specimens broke when the front pullout forces reached 850 N, meaning that the specimens reached tensile strength.

7.2 Effect of granulated rubber content on front pullout force–displacement curves

Figure 10 compares the front pullout force–displacement curves of different rubber contents (10%, 15% and 30%) under the normal pressures of 30 kPa, 50 kPa and 100 kPa, respectively. It could be observed that the front pullout forces increased faster in the cases of 15% rubber content than other two contents, and the front displacements required to mobilize the maximum front pullout forces were smaller in the cases of 15% rubber content than other two contents. The faster growth in front pullout force indicated that the geobelt–soil interaction in granulated rubber content of 15% was better than the other two contents. This conclusion coincides with the direct shear test results and demonstrates that there existed an optimal content for the best geobelt–soil interaction.

The existence of the optimal granulated rubber content for the best geobelt–soil interaction was also reported by some researchers. Tanchaisawat et al. (2010) investigated the interaction between geogrid and tire chip-sand backfill by various tests such as index tests, compaction tests, pullout tests, and large-scale direct shear tests, and concluded that the mixture of 30% mass ratio of tire chips was the most suitable fill material. Obviously, the optimal content of granulated rubber is closely related to multiple factors, including particle size distribution of granulated rubber and soil, compaction method, moisture content, temperature, etc.

7.3 Strain distribution of SEGB

Benefiting from the tensoresistivity of SEGB, the strain of geobelt could be calculated according to Eq. (1) by measuring the changes of electrical resistance. The tensoresistivity of SEGB could be utilized as a convenient method to conduct distributed measurements, and thereby to validate the numerical results of the strain distribution.

By investigating different moments in pullout process, the evolution of the strain distribution alongside the geobelt could be reflected. Since the strain of the geobelt is closely related to the tensile force, several front pullout force levels in pullout process are selected. Taking the granulated rubber content of 15%

Table 3 Cases of pullout test

Test amount	Normal pressure σ_v	Mass ratio of granulated rubber
9	30 kPa,50 kPa,100 kPa	10%, 15%, 30%

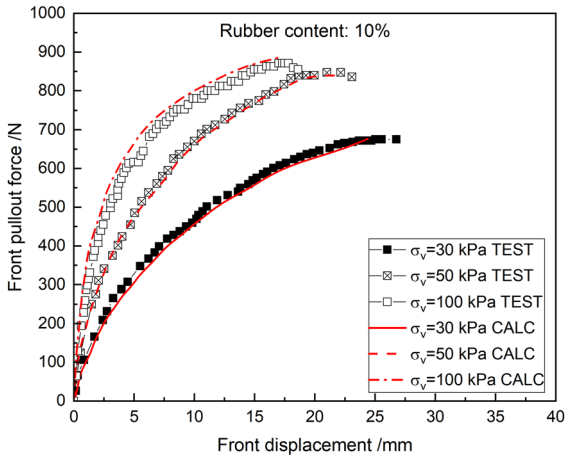

(a)

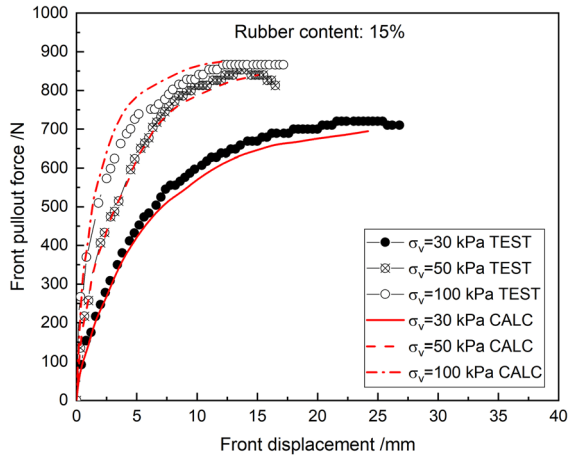

(b)

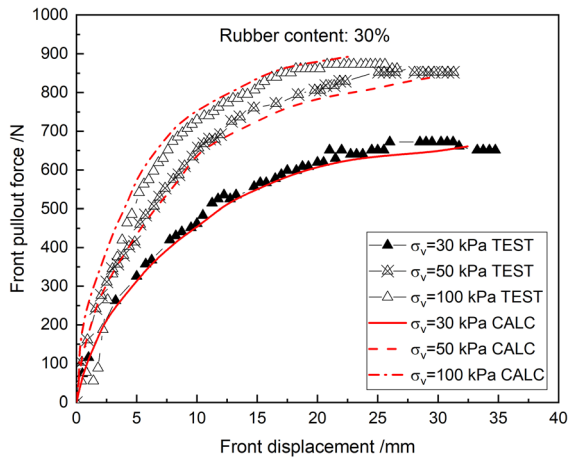

(c)

◀**Fig. 9** The comparisons of numerical and tested front pullout force–displacement curves with different rubber contents: **a** Rubber content: 10%; **b** Rubber content: 15%; **c** Rubber content: 30%

as an example, Fig. 11 shows the tested and numerical strain distributions with different normal pressures and front pullout force levels (50%, 75% and 100% of F_{0m}, and F_{0m} denotes the maximum value of front pullout force), respectively.

The consistency of the tested and numerical results could validate the pullout behavior model, including the bilinear model and the hyperbolic model. The deformation behaviour of SEGB in pullout process was also proved. The deformation of geobelt started from the front end, then progressively delivered towards the tail end. However, the strain level decreased rapidly along the geobelt in soil.

It is observed that the tested results were smaller than the numerical results at tail end zones. It is highly possible that the tested results were subjected to the sensitivity of the measurements. The sensitivity of the measurements here may refer to two aspects. One is related to the tensoresistivity of SEGB itself. It is possible that the deformation is so subtle that the electrical resistance is unchanged. This influence involves many factors such as the length of measuring zones and temperature. The other one is the insufficient sensitivity of measuring instruments, which is believed to be the major cause for the smaller tested results.

7.4 Distributions of tensile force, displacement and shear stress along the geobelt

It is inconvenient to acquire the deformations of geobelts inside soil with traditional methods of measurements. The tensoresistivity of SEGB could not only realize the distributed measurements of strain along the geobelts in soil, but also prove the validity of established load transfer equation and the Finite-differential method. The numerical solutions could give not only the strain distribution along the geobelts but also the distributions of tensile force, displacement and shear stress. Taking the granulated rubber content of 15% as an example, Fig. 12 shows the distributions of tensile force, displacement and shear stress from

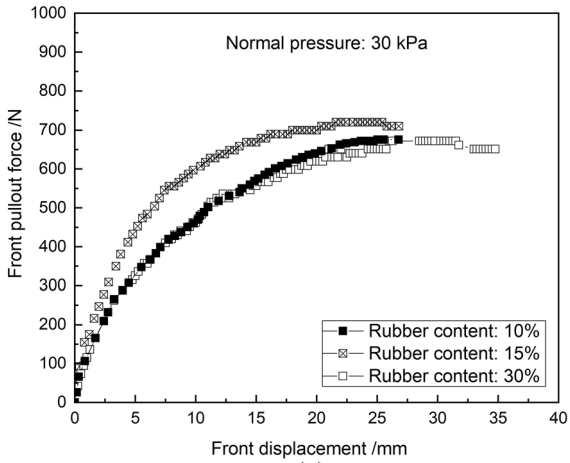

(a)

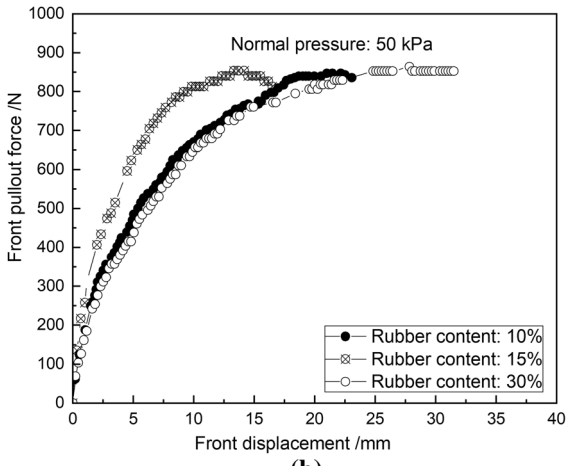

(b)

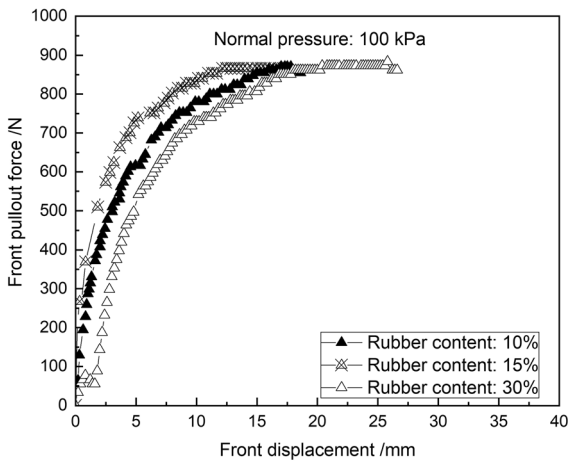

(c)

Fig. 10 The effect of rubber content on the front pullout force–displacement curves: **a** σ_v = 30 kPa; **b** σ_v = 50 kPa; **c** σ_v = 100 kPa

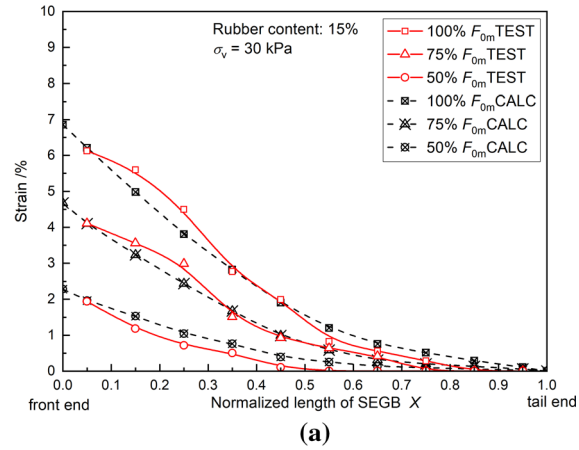

(a)

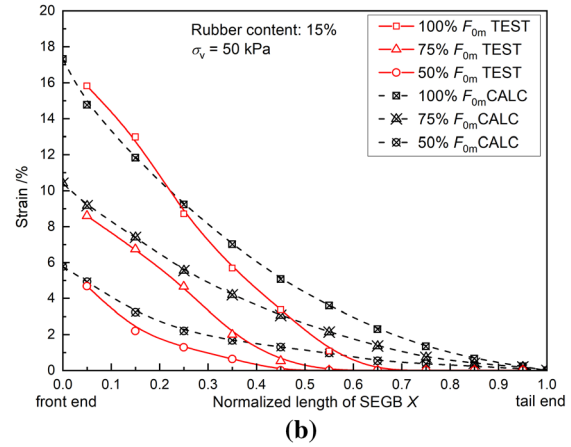

(b)

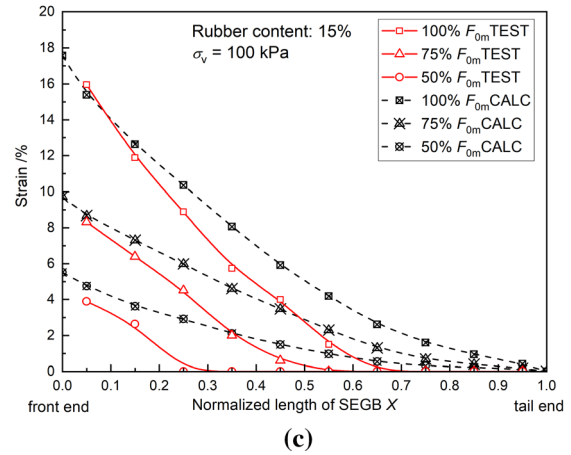

(c)

Fig. 11 Strain distribution of SEGB: **a** σ_v = 30 kPa; **b** σ_v = 50 kPa; **c** σ_v = 100 kPa

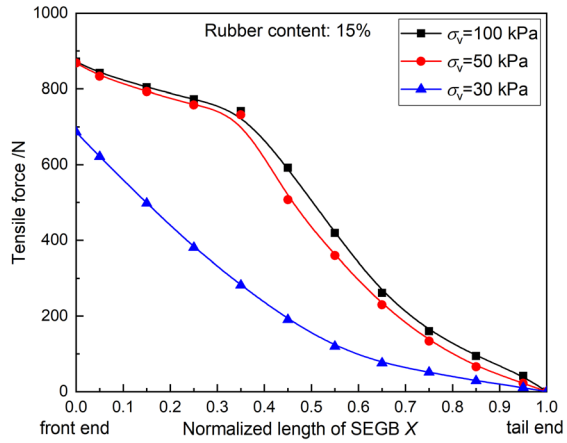

(a)

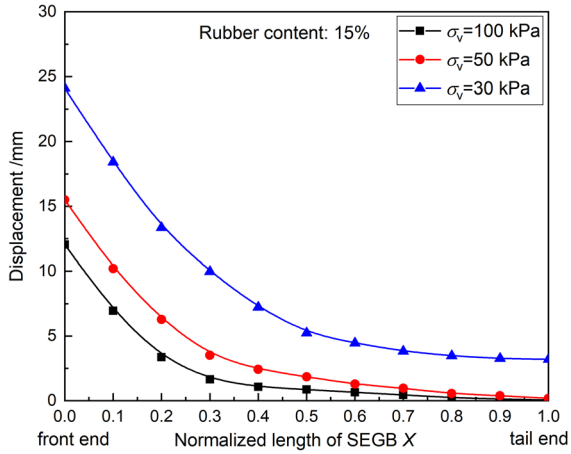

(b)

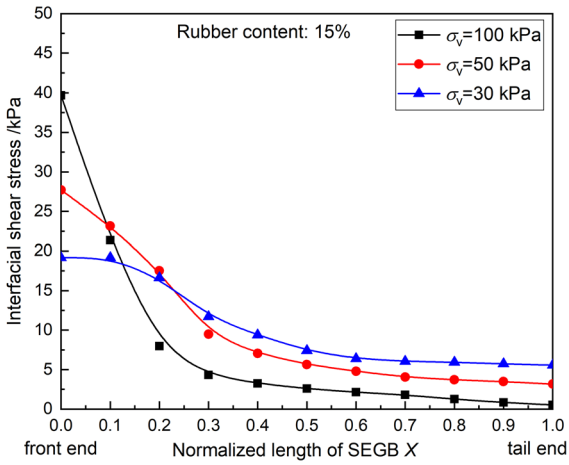

(c)

◀**Fig. 12** Numerical results (F_0 = 100% F_{0m}, granulated rubber content of 15%): **a** Tensile force distribution; **b** Displacement distribution; **c**Interfacial shear stress distribution

numerical solutions when the pullout force was 100% F_{0m}, respectively.

Figure 12a clearly indicates that the tensile force level generally increased with increasing normal pressure. The tensile forces reached the maximum value at the front end of geobelts, then decreased along the geobelts until zero at the tail end. In the cases of high normal pressures (50 kPa and 100 kPa), the tensile forces clearly showed piecewise distributions. Tensile force maintained at high levels in front part of geobelt and decreased slowly, indicating this part of geobelt exhibited quasi-plasticity; afterwards the tensile force decreased rapidly to zero, indicating the rest part of geobelt was quasi-elastic. However, in the case of low normal pressure (30 kPa), the tensile force was generally smaller than that of high normal pressures, and piecewise distribution was not observed neither, which indicated that the whole geobelt was quasi-elastic.

Figure 12b shows that the displacement level was generally lower under higher normal pressures. The displacement reached maximum value at the front end of geobelt, and decreased rapidly afterwards. In the case of low normal pressure (30 kPa), the tail end of geobelt had obvious displacement, indicating that the geobelt under normal pressure of 30 kPa was pulled out from confining soil. However, the tail end displacement was pretty small (close to zero) in the cases of high normal pressures (50 kPa and 100 kPa), which demonstrated the front end of geobelt reached tensile strength with little movement at tail end, indicating break failure of geobelts. The observations in pullout tests coincided with these judgements.

Figure 12c shows that the interfacial shear stress was related to normal pressure and the interfacial relative displacement both. Since sponges on the sleeve (as shown in Fig. 8) were placed to prevent the loss of soil particles, it is feasible to assume that the interfacial relative displacements were equivalent to geobelt displacements. The interfacial shear stress reached the maximum value at the front end of geobelt, and decreased afterwards until stabilized at the tail end. With higher normal pressures, the maximum values of interfacial shear stresses were

higher at the front end, but decreased faster afterwards and stabilized at lower levels at the tail end.

Compared to the breaking failure, the interfacial shear stress of geobelts with pullout failure (i.e., the geobelts with movements at the tail end) was much smaller but exhibited more uniform distribution—the difference between the maximum and minimum values was smaller. Some researchers (Zornberg et al. 2017) assumed the interfacial shear stress as a constant value, which was only feasible for the condition of low normal pressures or pullout failure cases.

7.5 Discussion

Enhanced by the interaction between geosynthetics and soil, GRS has gained reputation of excellent performances in terms of stability, bearing capacity and controlling deformations. Obviously the geosynthetic-soil interaction, especially the deformation of geosynthetics, is vital to the stability considerations. With the SEGB and the constitutive models presented in this paper, it is available to acquire the interfacial behaviour inside GRS, including the distributions of stress, displacement and interfacial shear stress. Further, the interfacial behavior of SEGB shows quantitative differences between two failure modes (pullout and break), it is possible to make preliminary judgement of potential failure in GRS, including the failure position on SEGB and the possible failure mode. The determination of interfacial behaviour would be valuable for the design, stability analysis, structural health monitoring and early warning of GRS.

8 Conclusion

This paper investigates the pullout behaviour of geobelts in weathered rock materials (WRM) mixed with different ratios of granulated rubbers. Two constitutive models—bilinear model capturing the full stress–strain response of geobelts and hyperbolic model simulating the geobelt–soil interaction are established based on the results of uniaxial tensile tests and direct shear tests, respectively. Load transfer equation for pullout process is deduced by incorporating the two constitutive models. Pullout tests that consider different granulated rubber contents (10%, 15% and 30%) in WRM and different normal pressures (30 kPa, 50 kPa and 100 kPa) are carried out based on a self-developed testing apparatus. Sensor-enabled geobelts (SEGB) are employed, which possess tensoresistivity and could realize distributed measurements on geobelt deformations. Conclusions could be drawn from the comparisons of numerical and tested results:

(1) The good agreement of the numerical and tested results proves the validity of the load transfer equation for the pullout process, including the two constitutive models—the bilinear model capturing the full stress–strain response of SEGB; and the hyperbolic model simulating the geobelt–soil interaction.
(2) There exists an optimal granulated rubber content for the best geobelt–soil interaction. For the granulated rubber content of 15%, the pullout forces have faster increment and the front displacements are smaller to reach the maximum pullout forces, indicating that 15% is the optimal granulated rubber content in this paper.
(3) The distributed measurements of SEGB elaborate the deformation behaviour of geobelts in pullout process. The deformation of geobelts starts from the front end, then progressively delivers towards the tail end. The deformation decreases rapidly along the geobelt in soil.
(4) The tensile force, displacement and interfacial shear stress of geobelt all reach the maximum values at the front end of geobelts, then decrease along the geobelts until stabilize at the tail end. The geobelts under high normal pressures exhibit quasi-plasticity with high levels of strain but low levels of displacement. The distributions of interfacial shear stresses along geobelts are more uniform under low normal pressures than high normal pressures.

Acknowledgements This work is supported by the National Key Research and Development Program (2018YFB1600100), the Natural Science Foundations of China (No. 51778346), and the Key Research and Development Program of Shandong Province (2017GGX50102; 2019GSF111007).

References

Abdelouhab A, Dias D, Freitag N (2010) Physical and analytical modelling of geosynthetics strip pull-out behavior. Geotext Geomembr 28:44–53

Anastasiadis A, Senetakis K, Pitilatis K (2012) Small-strain shear modulus and damping ratio of sand-rubber. Geotech Geol Eng 30:363–382

Argyroudis S, Palaiochorinou A, Mitoulis S, Pitilakis D (2016) Use of rubberised backfills for improving the seismic response of integral abutment bridges. Bull of Earthq Eng 14:3573–3590

ASTM International (2001) Standard test methods for geosynthetics, ASTM D6637–01(2001). ASTM International, West Conshohocken, PA. https://doi.org/10.1520/D6637-01

ASTM International (2007) Standard test method for particle-size analysis of soils, ASTM D422–63(2007) e2. ASTM International, West Conshohocken, PA. https://doi.org/10.1520/D0422-63R07E02

ASTM International (2013) Standard test method for measuring geosynthetic pullout resistance in soil, ASTM D6706–01(2013). ASTM International, West Conshohocken, PA. https://doi.org/10.1520/D6706-01R13

ASTM International (2017) Standard practice for use of scrap tires in civil engineering applications, ASTM D6270–17(2017). West.Conshohocken, PA: ASTM International, 10.1520/D6270–17

ASTM International (2019) Standard test method for determining the shear strength of soil-geosynthetic and geosynthetic-geosynthetic interfaces by direct shear, ASTM D5321/D5321M-19(2019). ASTM International, West Conshohocken, PA. https://doi.org/10.1520/D5321_D5321M-19

Attom MF (2006) The use of shredded waste tires to improve the geotechnical engineering properties of sands. Environ Geol 49:497–503

Balunaini U, Yoon S, Prezzi M, Salgado R (2014) Pullout response of uniaxial geogrid in tire shred–sand mixtures. Geotech Geol Eng 32:505–523

Bernal A, Salgado R, Swan RH, Lovell CW (1997) Interaction between tire shreds, rubber–sand and geosynthetics. Geosynth Int 4:623–643

Bosscher PJ, Edil TB, Kuraoka S (1997) Design of highway embankments using tire chips. J Geotech Geoenviron Eng 123:295–304

Chai JC, Saito A (2016) Interface shear strengths between geosynthetics and clayey soils. Int J Geosynth Ground Eng 2:19

Chari TR, Meyerhof GG (1983) Ultimate capacity of rigid single piles under inclined loads in sand. Can Geotech J 20:849–854

Chawla S, Shahu JT (2016) Reinforcement and mud-pumping benefits of geosynthetics in railway tracks: model tests. Geotext Geomembr 44:336–380

Chen Q, Abu-Farsakh M (2016) Mitigating the bridge end bump problem: a case study of a new approach slab system with geosynthetic reinforced soil foundation. Geotext Geomembr 44:39–50

Chen RP, Wang YW, Ye XW, Bian XC, Dong XP (2016) Tensile force of geogrids embedded in pile-supported reinforced embankment: A full-scale experimental study. Geotext Geomembr 44:157–169

Cui XZ, Wang L, Cui SQ, Wang YL, Wang ZX, Zhang L, Su JW, Xiao M (2017) Laboratory tests on permeability of TDA-weathered rock material mixtures. In: International conference on transportation infrastructure and materials. Qingdao, Shandong, China, June 2017

Cui XZ, Cui SQ, Jin Q, Wang YL, Zhang L, Wang ZX (2018a) Laboratory tests on the engineering properties of sensor-enabled geobelts (SEGB). Geotext Geomembr 46:66–76

Cui XZ, Cui SQ, Wang YL, Li J (2018b) "Laboratory tests on the engineering properties of sensor-enabled geobelts (SEGB)"- A reply to the discussion. Geotext Geomembr 46:681–683

Duncan JM, Chang CY (1970) Non-linear analysis of stress and strain in soils. J Soil Mechanics Found Divsion 96:1629–1653

Ghazavi M (2004) Shear strength characteristics of sand-mixed with granular rubber. Geotech Geol Eng 22:401–416

Gurung N (2001) 1-D analytical solution for extensible and inextensible soil/rock reinforcement in pull-out tests. Geotext Geomembr 19(4):195–212

Gurung N, Iwao Y (1999) Numerical simulation of pullout response for planar soil reinforcements. Can Geotech J 36:455–466

Hatami K, Grady B, Ulmer M (2009) Sensor-enabled geosynthetics: use of conducting carbon networks as geosynthetic sensors. J Geotech Geoenviron Eng 135:863–874

Huang D (2017) Laboratory experimental study on geotechnical properties of tire-derived aggregate-weathered rock material mixtures (in Chinese). Dissertation, Shandong University 48:118–123

Infante DJU, Martinez GMA, Arrua PA, Eberhardt M (2016) Shear strength behavior of different geosynthetic reinforced soil structure from direct shear test. Int J Geosynth Ground Eng 2:17

Li J, Cui XZ, Jin Q, Su JW, Cui SQ, Wang YL (2018) Laboratory investigation of the durability of a new smart geosynthetic material. Constr Build Mater 169:28–33

Liu HB (2016) Nonlinear elastic analysis of reinforcement loads for vertical reinforced soil composites without facing restriction. J Geotech Geoenviron Eng 142(6):040160131–40160139

Liu HB, Yang GQ, Hung C (2017) Analyzing reinforcement loads of vertical geosynthetic-reinforced soil walls considering toe restraint. Int J Geomech 17(6):04016140

Madhav MR, Gurung N, Iwao Y (1998) A theoretical model for the pull-out response of geosynthetic reinforcement. Geosynth Inter 5(4):399–424

Punetha P, Mohanty P, Samanta M (2017) Microstructural investigation on mechanical behavior of soil-geosynthetic interface in direct shear test. Geotext Geomembr 45:197–210

Racana N, Grediac M, Gourves R (2003) Pull-out response of corrugated geotextile strips. Geotext Geomembr 21:265–288

Rousé PC, Fannin RJ, Taiebat M (2014) Sand strength for back-analysis of pull-out tests at large displacement. Géotechnique 64(4):320–324

Sadat Taghavi SH, Mosallanezhad M (2017) Experimental analysis of large-scale pullout tests conducted on polyester anchored geogrid reinforcement systems. Can Geotech J 54:621–630

Shahin HMD, Nakai T, Morikawa Y, Masuda S, Mio S (2017) Effective use of geosynthetics to increase bearing capacity of shallow foundations. Can Geotech J 54:1647–1658

Shen P, Xu C, Han J (2018) Model tests investigating spatial tensile behavior of simulated geosynthetic reinforcement material over rigid supports. J Mater Civ Eng. https://doi.org/10.1061/(ASCE)MT.1943-5533.0002156

Shrestha S, Ravichandran N, Raveendra M, Attenhofer JA (2016) Design and analysis of retaining wall backfilled with shredded tire and subjected to earthquake shaking. Soil Dyn Earthq Eng 90:227–239

Tanchaisawat T, Bergado DT, Voottipruex P, Shehzad K (2010) Interaction between geogrid reinforcement and tire chip–sand lightweight backfill. Geotext Geomembr 28:119–127

Tafreshi SM, Khalaj O, Dawson AR (2014) Repeated loading of soil containing granulated rubber and multiple geocell layers. Geotext Geomembr 42:25–38

Tavakoli MG, Ghanbari A, Mehdizadeh H (2016) Experimental study on the behaviour of geogrid-reinforced slopes with respect to aggregate size. Geotext Geomembr 44:862–871

Wang L, Chen G, Chen S (2015) Experimental study on seismic response of geogrid reinforced rigid retaining walls with saturated backfill sand. Geotext Geomembr 43:35–45

Wang Z, Jacobs F, Ziegler M (2016) Experimental and DEM investigation of geogrid-soil interaction under pullout loads. Geotext Geomembr 44:230–246

Yu Y, Bathurst RJ (2017) Influence of selection of soil and interface properties on numerical results of two soil–geosynthetic interaction problems. Int J Geomech 17(6):04016136

Yu Y, Bathurst RJ, Allen TM, Nelson R (2016) Physical and numerical modelling of a geogrid-reinforced incremental concrete panel retaining wall. Can Geotech J 53(12):1883–1901

Zhang F, Gao Y, Leshchinsky D, Yang S, Dai G (2018) 3D effects of turning corner on stability of geosynthetic-reinforced soil structures. Geotext Geomembr 46:367–376

Zornberg JG, Roodi GH, Gupta R (2017) Stiffness of soil-geosynthetic composite under small displacements: i model development. J Geotech Geoenviron Eng 143(10):04017075